Geophysical Research Letters

Key Points:
- We use satellite imagery and ICESat-2 repeat-track data to examine a large tabular calving event from Amery Ice Shelf in September 2019
- ICESat-2 repeat tracks reveal rift structures with uplifted flanking walls that appear to modulate future ice front shape
- ICESat-2 reveals the subtle topographic signatures of active rifts, even beyond the limit where they are visible in satellite imagery

Correspondence to:
C. C. Walker,
cwalker@whoi.edu

A High Resolution, Three-Dimensional View of the D-28 Calving Event From Amery Ice Shelf With ICESat-2 and Satellite Imagery

Catherine C. Walker[1] , **Maya K. Becker**[2] , and **Helen A. Fricker**[2]

[1]Department of Applied Ocean Physics and Engineering, Woods Hole Oceanographic Institution, Woods Hole, MA, USA, [2]Institute of Geophysics and Planetary Physics, Scripps Institution of Oceanography, University of California, La Jolla, San Diego, CA, USA

Abstract Tabular calving events occur from Antarctica's large ice shelves only every few decades, and are preceded by rift propagation. We used high-resolution imagery and ICESat-2 data to determine the propagation rates for the three active rifts on Amery Ice Shelf (AIS; T1, T2, and E3) and observe the calving of D-28 on September 25, 2019 along T1. AIS front advance accelerated downstream of T1 in the years before calving, possibly increasing stress at the rift tip. T1 experienced significant acceleration for 12 days before calving, coinciding with a jump in propagation of E3. ICESat-2's high resolution and repeat acquisitions every 91 days allowed for analysis of the ice front before and after calving, and rift detection where it was not visible in imagery as a ~1 m surface depression, suggesting that it propagates as a basal fracture. Our results show that ICESat-2 can provide process-scale information about iceberg calving.

Plain Language Summary Antarctica's ice shelves surround the ice sheet where it meets the ocean, and modulate the flow of grounded ice. Ice shelves lose the mass they gain through snowfall via two main processes: calving of icebergs at the front, and melting underneath. If losses exceed gains, they shrink, and the glaciers feeding them will feel less resistance to flow and speed up, and sea level will rise. Overall, Antarctica's ice shelves are experiencing excess mass loss; however, the ice sheet is losing mass only in key sectors, and the large ice shelves are mostly in equilibrium. For those ice shelves, large calving events are normal "background" mass loss processes. However, since they occur infrequently (only every few decades) we have not had many events to study with modern, high spatial resolution satellite data. Antarctica's third largest ice shelf, Amery Ice Shelf, calved a tabular iceberg in September 2019, providing an opportunity for a detailed process study of iceberg calving. We use satellite imagery and ICESat-2 altimetry data to look at the precursors to calving and the effect of the calving event on the ice shelf. This will inform models about the calving process.

1. Introduction

Antarctica's ice shelves regulate the flow of grounded ice from the continent, via a process known as buttressing (Thomas et al., 1979). Under stable climate conditions, ice shelves remain in approximately steady state; they gain mass from ice flow across the grounding line and snowfall, and lose mass through ocean melting at their bases, episodic iceberg calving from their ice fronts, surface sublimation, and seasonal surface melting. Overall, basal melting and calving account for approximately equal amounts, but individual ice shelves have different ratios (Rignot et al., 2013). Since the 1990s, ice shelves have been losing net mass overall (Adusumilli et al., 2020; Paolo et al., 2015), leading to increased grounded ice flow rates (Gudmundsson et al., 2019). This excess mass loss has been attributed to increased ocean-driven melting, the main mass loss process occurring in the regions undergoing change. On large ice shelves, however, calving is the dominant mass loss process (Rignot et al., 2013). These ice shelves are mostly in equilibrium, and lose most of their mass via large tabular calving events.

Tabular iceberg calving involves the initiation and propagation of crevasses and rifts, and this process is key to understanding stress balances in ice shelves (Bassis et al., 2008; Fricker et al., 2005a; Walker et al., 2013). Rift propagation can occur over timescales from days to decades prior to calving (e.g., Benn & Åström, 2018). Satellite imagery has enabled monitoring of rift propagation and its variability over increasingly long periods. Studies of the calving process have focused on understanding the factors that control the propagation

of rifts (e.g., Bassis et al., 2005, 2008; Benn et al., 2007; Fricker et al., 2005; Heeszel et al., 2014; Hulbe et al., 2010; Larour et al., 2004; MacGregor et al., 2012; Walker et al., 2013, 2015), some of which have suggested that surface environmental factors such as temperature and wind speed are not necessarily drivers (Humbert & Steinhage, 2011; Larour et al., 2004; Joughin & MacAyeal, 2005). Other studies have argued that ocean stresses, such as storm-induced swell, infra-gravity waves and tsunamis might drive rift propagation (Bromirski et al., 2010; K. Brunt et al., 2011; Lipovsky, 2018; MacAyeal et al., 2006, 2017; Sergienko, 2010). Walker et al. (2013) showed that rift behavior can generally be classified as "dormant," "sudden burst," "intermittently active," or "continuously active." The majority of large ice shelf rifts in Antarctica are dormant. Fricker et al. (2005) used ICESat data to map the vertical structure of ice shelf rifts and their evolution, and Walker and Gardner (2019) showed that active and dormant rifts have different topographic signatures in altimetry data.

Given the variety of timescales over which ice shelf rifts propagate, resultant iceberg calving is sporadic. These events only occur every few decades, and as such there have not been many opportunities to study them in detail over the satellite record. The recent (September 25, 2019) calving of the "Molar Iceberg" D-28 from Amery Ice Shelf (AIS) provides an opportunity to analyze satellite remote sensing data, and in particular ICESat-2 data, over the ice front and rifts before, during, and after a large tabular calving event. It is also the first large calving event to occur during ICESat-2's lifetime. Here, we present a perspective of the event using before-and-after observations from ICESat-2 and visible satellite imagery to characterize precursory and post-calving topographic changes related to the calving of D-28.

2. Amery Rift System

AIS is the largest East Antarctic ice shelf, and Antarctica's third-largest ice shelf overall. The last major calving event occurred in late 1963/early 1964 (Budd, 1966; Fricker et al., 2002) and as it advanced past its pre-calved position, six rifts opened in the ice front (Walker et al., 2013). Two small longitudinal-to-flow rifts on the western side of the ice front, W1 and W2, opened in the early 2000s (Ibid). Large longitudinal-to-flow rifts, L1 and L2, initiated in the late 1980s. L2 propagated until the early 1990s. Around 1995, L1 bifurcated into two transverse rifts (T1 and T2), forming a triple junction. At the eastern AIS margin, E3 originated as a marginal crevasse around 1996. Its propagation appears to be controlled by pre-existing crevasses in its vicinity (Figure 1a). T1, T2, and E3 were actively propagating throughout the last 2 decades (e.g., Bassis et al., 2005, 2008; Fricker et al., 2002; Walker et al., 2015). L1, T2, and L2 define AIS's "Loose Tooth" system, which had been predicted to calve an iceberg in the next decade or so (Fricker et al., 2002). Instead, iceberg D-28 separated along T1 between September 24 and 25, 2019 (Figure 1a). Upon calving, D-28 was estimated to be about 210 m thick and contained ∼315 billion tonnes of ice (ice draft map from Adusumilli et al. [2020]). Since calving, D-28 has drifted westward and as of December 2020 is floating offshore of Enderby Land, ∼990 km from its origin.

Early observations of AIS rift propagation were obtained by Fricker, Young et al., (2005) using satellite imagery to create an 8-year time series (1996–2004). These data suggested a seasonal trend with faster propagation rates in Austral summer than in Austral winter. Subsequent field studies supported this and concluded that environmental drivers may increasingly trigger rift propagation as an iceberg becomes closer to detachment (Bassis et al., 2008). A later study of AIS rift propagation from 2002 to 2015 found that the timing of propagation events correlated with sustained winds (>4 days), along with the arrival of tsunamis (Walker et al., 2015). However, for the most part, propagation was controlled by structural conditions in the AIS, for example rifts being front-initiated (open to ocean impact), the presence of crevasses, proximity to other actively propagating rifts, and suture zones (Walker et al., 2013; 2015).

3. Data and Methods

3.1. Rift Lengths and Velocities From Satellite Imagery

3.1.1. Landsat Imagery and Derived Velocities

We used visible imagery from two sources to analyze the AIS rift extents. The Landsat 8 Operational Land Imager imagery has 15 m resolution in the panchromatic band (Band 8), and WorldView-3 multi-spectral imagery from DigitalGlobe has a spatial resolution of 1.24 m.
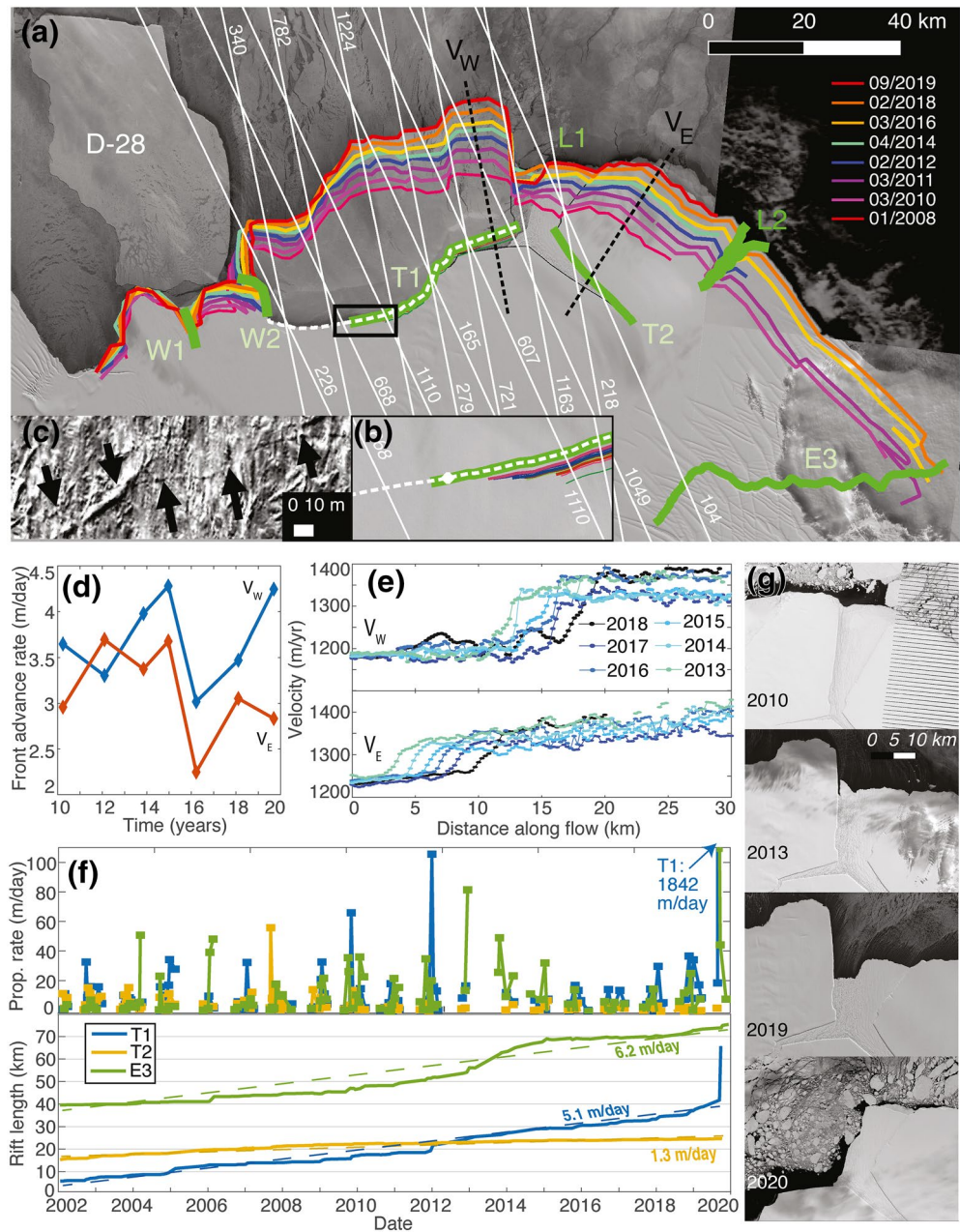
Figure 1. Amery Ice Shelf front before and after calving of D-28. (a) A view of the AIS ice front pre-calving (Landsat, September 12, 2019) with a shadowed image of the AIS post-calving (Landsat, October 5, 2019, marked D-28). Map shows the five active rifts in the AIS at their September 2019 locations (green). White lines show ICESat-2 RGTs. Color lines show calving front positions since 2008 (labeled top right). Black dotted lines labeled VW and VE show velocity measurement locations in (d and e). (b) Zoomed-in view (black box, a) of the rift tip at its last visible location on September 12 (green); white dotted line shows eventual path to isolate iceberg D-28. (c) Worldview-3 image (copyright 2020 DigitalGlobe, Inc.) from September 4, 2019 of the resolvable surface crack (black arrows) ~1 m across; white square on (b) shows location magnified 10X. (d) The frontal advance rate measured at the ice front along V_W and V_E in (a). (e) Velocity fields 2013–2018 along the lines shown in (a) to demonstrate the velocity jump across T1 (top) and T2 (bottom). (f) (bottom) Rift lengths measured from MODIS (2002–2015) and Landsat (2013–2020) imagery, and mean daily propagation rate (top). (g) Landsat images from March 2010, 2016, 2019, and September 2020 showing change in L1 mélange extent.

We used Landsat-derived ice surface velocities from the Inter-mission Time Series of Land Ice Velocities and Elevation (ITS_LIVE) data set (Gardner et al., 2019) to determine flow regime near the ice front. Details of this data set are provided in the ITS_LIVE Regional Glacier and Ice Sheet Surface Velocities user documentation (Gardner et al., 2019).

3.1.2. Determination of Rift Propagation Rates

We determined rift lengths and propagation rates in AIS through April 2020, building upon previous work for the period 2002–2015 by Fricker et al. (2005) and Walker et al. (2015). The length of each rift was measured in cloud-free images following the methodology in Walker et al. (2013). We defined the "rift tip" as the final point at which a rift pixel is discernible from the background after contrast stretching. Thus, it may be that the true rift tip extends farther than can be resolved in Landsat panchromatic images if the rift becomes narrower than a single pixel (∼15 m). Our measurements reflect that, we are only able to discern the rift's surface expression; we could not observe subsurface propagation or rift tips obscured by snow. Our estimated precision in Landsat imagery is ∼2 pixels (30 m). Visible imagery limited these observations to the Austral summer. We estimated rift propagation rates by dividing length changes by the number of days between measurements.

We made measurements for the period 2013–2020, and combining the times series' of Fricker et al. (2005) and Walker et al. (2015), produced an 18-years time series (2002–2020). Because the earlier 2 time series' used Moderate Resolution Imaging Spectroradiometer (MODIS) and Multi-angle Imaging Spectroradiometer (MISR) imagery, we anticipated a measurement bias between the two datasets due to resolution differences (15 m for Landsat 8 vs. 275 m for MISR and 250 m for MODIS). Thus we repeated measurements between 2013 and 2015 from Walker et al. (2015) using contemporaneous Landsat 8 imagery, and adjusted the 2002–2015 time series accordingly.

3.1.3. Determination of Frontal Advance Rate

To determine variability in advance rate of the ice front downstream of T1 and T2, we manually traced ice front positions where the ice front was cloud-free (Figure 1a). We characterized the forward motion of the front over time by measuring distance traveled parallel to flow (Section 3.1.4), along the eastern and western portions of the front (black lines, V_W and V_E, Figure 1a). The "frontal advance rate" was determined by dividing the change in distance by time between observations.

3.1.4. Determination of Ice Flow Rates

We used annual velocities between 2013 and 2018 from the ITS_LIVE data set to determine changes in flow near the AIS front. We used the *x*- and *y*-component of velocity, estimated at 240 m resolution, to determine the "along-flow" motion of both sides (V_W and V_E, Figure 1a). We extracted velocity profiles in the along-flow direction for the western (V_W across T1) and eastern (V_E across T2) sections of the ice front region.

3.2. Rift Topography From ICESat-2 Altimetry

3.2.1. ICESat-2 ATLAS

ICESat-2 launched in September 2018 and thus has recently begun to provide unprecedented views of Antarctic ice shelf rifts (e.g., Smith et al., 2020a; Walker & Gardner, 2019). ICESat-2 carries the Advanced Topographic Laser Altimeter System (ATLAS), a photon-counting, 532 nm lidar. ATLAS operates at 10 kHz and splits the transmitted laser pulse into six beams to form three pairs (composed of one weak and one strong beam, separated by 90 m) spaced 3.3 km apart. Each beam has a ground-footprint ∼17 m in diameter, offset by 0.7 m along-track. ATLAS collects data along 1,387 unique Reference Ground Tracks (RGTs) on Earth's surface. ICESat-2's polar orbit extends to 88°, and its 91-days repeat cycle allows for sampling four times per year. Observations along RGTs covered between October 2018 and March 2019 (Cycle 1 and some of Cycle 2) occurred prior to the on-orbit pointing calibrations being determined and updated within the on-board pointing control systems (Martino et al., 2019). As such, observations from those dates do not represent repeat tracks. We primarily use the Level 3A Land Ice Height (ATL06) Release 003 (Smith et al., 2020b), supported by the Level 2A Global Geolocated Photon Data (ATL03) Release 003 data product (Neumann

et al., 2020). Over the ice sheets, ATLAS has been shown to have a surface precision of better than 13 cm (K. M. Brunt et al., 2019).

3.2.2. Determining Rift, Mélange and Ice Front Topography From ICESat-2 Height Data

We used ICESat-2 ATL06 data to examine pre- and post-calving ice front and rift topography, and to determine the utility of ATL06 in detecting rift propagation during the austral winter when visible imagery is not available. The ice front area is covered by several RGTs (Figure 1a), and the data we used are from Cycle 2 (started December 28, 2018) through Cycle 6 (ended March 26, 2020). ATLAS was in safe-hold between June 26 and July 9, 2019, during which ATLAS did not collect data; thus, RGTs 0104 and 0165 were not sampled in July 2019. Available ATL06 granules over the five cycles were downloaded and checked for cloud flag values over the area of interest. To ensure we did not automatically throw out usable data based only on the cloud flag value, we determined the average surface height over the area of interest. If it was greater than 200 m (much higher than the expected surface elevation in the area, ∼50–70 m), we deduced that clouds covered the study site. More than half of available granules during the study period were significantly cloudy enough that we could not distinguish the surface near the rift. For clear measurement days, the mean slope of the ice shelf was removed by fitting a first-order polynomial and subtracting it from the ICESat-2 elevation to isolate the rift topography profile.

4. Results and Discussion: Satellite-Derived Observations of Rift Propagation and Ice Front Structure

4.1. Rift Propagation From Imagery

The rift length time series showed T1, T2, and E3 following similar trends as detected previously (Walker et al., 2015). Between 2002 and 2019, T2 propagated at a mean rate of 1.2 ± 0.04 m/day. Around Austral winter 2010, T2 shifted to a lower propagation rate and maintained that slower pace since then, lacking any large propagation events (>10 m/day, Figure 2a) after 2010.

The two westward-propagating rifts maintained their faster propagation rates since last observed (Walker et al., 2015). Rift E3 propagated fastest overall at an average of 6.2 ± 0.04 m/day between 2002 and 2020. In April 2013, E3 turned south, along-flow. This turn coincided with the collision of an iceberg from the Polar Times Glacier with E3's downstream rift wall. This correlated with a speedup from Austral winter 2013 through early 2015 before E3 returned to its pre-impact rate. E3 experienced the greatest number of large events (>10 m/day, Figure 1f) throughout the observation period.

T1 propagated at an average rate of 5.1 ± 0.04 m/day (Figure 1f). Large propagation events for T1 occurred with a particular cadence; propagation events were small in Austral spring, grew larger in mid-summer, and returned to smaller magnitudes around March-April. This was not observed in T2 or E3. The two largest events in T1's lifetime occurred in early 2012 and in late 2019. Prior to 2012, T1 had propagated to the edge of the main AIS suture zone and slowed as it propagated through it. The increase in propagation rate in March 2012 occurred as T1 propagated through to the other side of the marine-ice filled suture zone, an ice shelf feature that may have a stabilizing effect (Borstad et al., 2017; Kulessa et al., 2014, 2019). This breakthrough also coincided with the shift in frontal advance rate between 2012 and 2013 (Figure 1d). At that point, the portion of the ice front downstream of T1 began advancing faster than that downstream of T2.

The second significant propagation event in T1 occurred in September 2019, when T1 propagated ∼23 km (∼1842 ± 19 m/day) from its last observed position on 12 September to connect with W2 and isolate iceberg D-28 on 25 September 2019. We found the timing of propagation of AIS rifts to be well correlated with occurrences of sustained high wind events (>4 days, see supporting information), consistent with previous findings by Walker et al. (2015). Therefore, this large propagation burst may be related to strong winds. Indeed, Francis et al. (2020) suggested that the D-28 calving event might have been linked to the removal of sea ice due to strong offshore winds, driven by anomalous twin polar cyclones over the AIS front. This is further supported by the observation that the T1 calving coincided with a relatively large propagation burst in rift E3 (Figure 1f, ∼110 m/day) between those same dates.
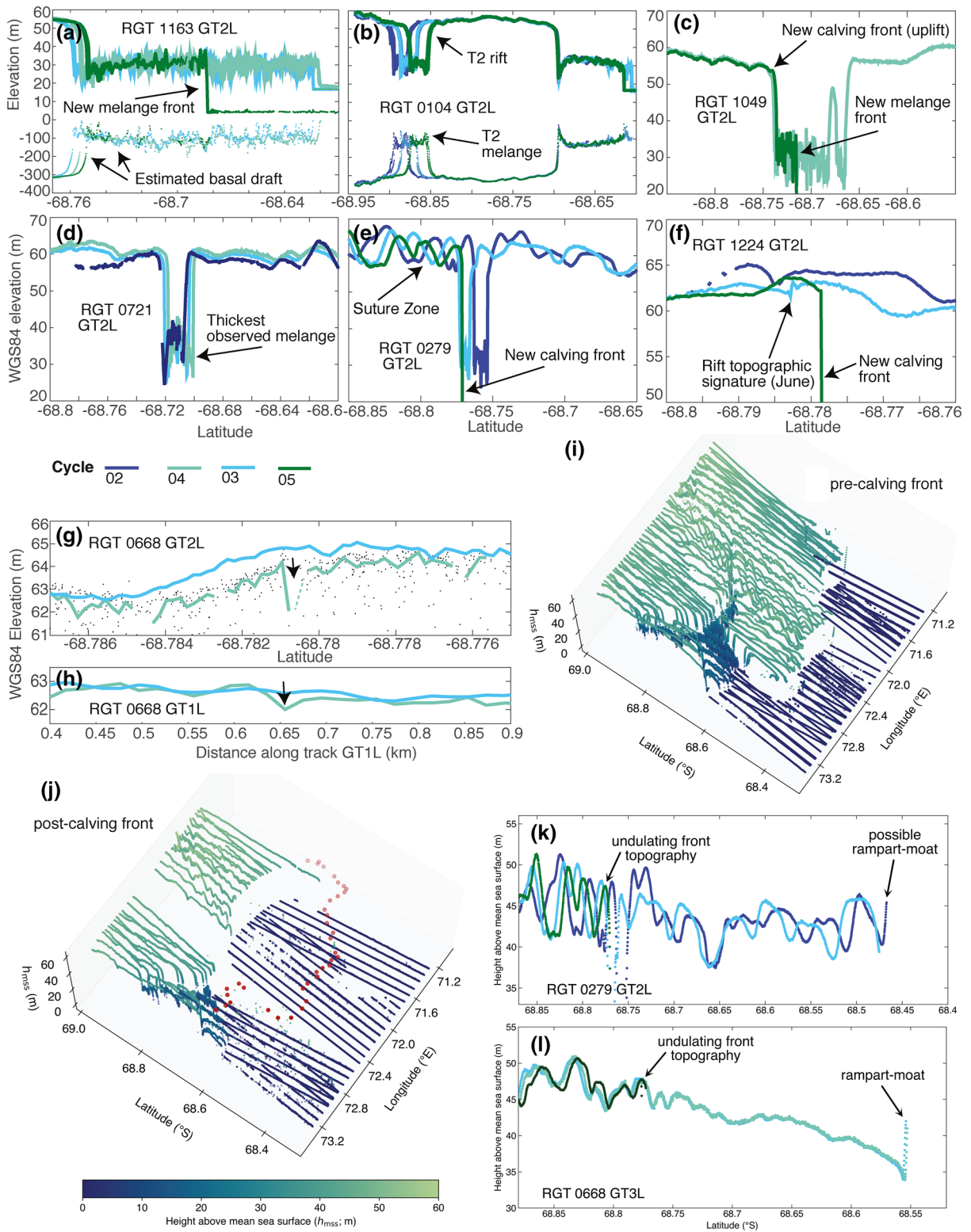
4.2. Flow Velocities and Frontal Advance

Velocity profiles (Figure 1e) show the change in velocity across each rift. Across T1, upstream ice moved ~125–175 m/year slower than ice ahead (downstream) of the rift. Ice upstream of T2 moved ~100–150 m/year slower than the ice downstream of the rift. Thus the increase across T1 is elevated relative to T2, and the distance over which the speedup occurs in T1 is shorter. The speed ramp-up is smoother across T2 than T1, likely related to the faster widening rate (divergence) observed at T1 by Walker and Gardner (2019). The slower widening rate at T2 suggests that the intra-rift mélange is more cohesive, providing a more continuous surface across which velocity change is absorbed. This suggests that the T1 rift and its mélange are more differentiated from the surrounding ice, allowing for increased freedom of movement of the future D-28. We find that the frontal advance rate ahead of T1 began to exceed that of the ice front downstream of T2 in 2012 (Figure 1d), which coincided with the propagation of T1 through the main suture zone in AIS. Both fronts experienced a slowdown in 2016, but since then the western front ahead of T1 has advanced more rapidly.

4.3. Local Rift, Mélange and Ice Front Changes before and After Calving

4.3.1. Changes in Mélange

Imagery revealed a significant change in spatial extent of the mélange in L1 (triple junction region) over the last decade (Figure 1g), initially suggesting a possible decrease in mélange strength related to thinning. We examined this for the year before calving. Acquisitions along RGT 1163 of the central mélange of the triple junction region showed that mean mélange thickness actually remained constant (~30 m above sea level with a draft of ~150 m), though those acquisitions do show that approximately half of the mélange area within L1 collapsed during the calving event (Figure 2a). One year post-calving (September 2020) the remainder of the former L1 mélange area remained at ~90% of its immediate post-calving area (Figure 1g). Mean mélange thickness in T2 also remained constant (~35 m above sea level with a draft of ~120 m) for the three acquisitions of RGT 0104 (Figure 2b) in January (pre-pointing correction), April, and October (post-calving). This thickness actually increased since its detection by ICESat in 2003 when it was estimated to have a draft of ~less than 100 m (Fricker et al., 2005a). We observe that the calving did not appear to have induced a mechanical response in T2 or its intra-rift mélange (Figure 2b, labeled). Based on repeat acquisitions of RGT 1049 in September (pre-calving) and December (post-calving), the mélange thickness in the triple-junction did not change significantly after calving, and one year post-calving this portion of the former intra-rift mélange remained in place (Figure 2c). Sampling along RGT 0721 (Figure 2f) showed that T1 widened, but intra-rift mélange thickness did not significantly change at that location either prior to the calving event. We hypothesize that this might suggest a process (freezing, infill, and/or redistribution) that balances mélange thickness as it spreads out in the widening rift on monthly-to-annual timescales. This segment of the rift was located ~3 km from the suture zone, and its mélange was the thickest observed anywhere in T1, T2, or L1, with surface elevations 3–6 m higher than the mean surface elevation of mélange in T2 or L1.

Paired with the observation of a more cohesive mélange within T2 using velocity records, and the lack of spatial change in the former T1 intra-rift mélange post-calving, we hypothesize that the eventual D-28 iceberg must have been mostly decoupled from the intra-rift mélange; with little resistance from the mélange it was able to tear away at an increasing rate of speed. This hypothesis is further supported by a similar observation at E3, the other fast-propagating rift in AIS, where intra-rift mélange is thin and broken enough to occasionally show open water. These observations suggest that mélange-ice wall coupling and strength (or lack thereof) may be a passive driver of rift propagation.

Figure 2. ICESat-2 observations of rifts, mélange and the ice front before and after calving. The surface and derived ice base across (a) L1 mélange (RGT 1163) and (b) T2 and L1 mélange (RGT 0104); (c) Surface height across the widest section of T1 (RGT 1049); (d) T1 and rift wall uplift pre-calving, showing the thickest mélange (RGT 0721, 0165); (e) T1 near its crossing of the suture zone, also showing rift wall uplift pre-calving and a similar wall shape post-calving (RGT 0279); (f) western-most track over the visible rift pre-calving showing a slight uplift matching the shape at the new ice front post-calving (RGT 1224); (g) RGT 0688 repeat across the future iceberg calving boundary, detecting a shallow surface depression (black arrows; shown here in ATL06 and ATL03 [black dots] in GT2L; and ATL06 for GT1L [h]). (i) Pre-calving ice shelf front captured by ICESat-2 in cycles 02/03/04, with both T1 and instances of buoyancy-driven front uplift visible; (j) post-calving ice front (cycles 05/06) exhibit similar morphology as the poleward wall of T1 in (i), with pre-calving front (red circles) for comparison; zoomed-in view of pre- and post-calving front shape and near-front topography along (k) RGT 0279 and (l) RGT 0668. RGT, reference ground tracks.

4.3.2. Changes in Rift Topography

In each location sampled pre-calving by ICESat-2 repeats, we observed uplifted rift wall flanks along active rift segments, as observed for AIS rifts using ICESat (Fricker et al., 2005) and on Filchner, Ross and Pine Island Glacier ice shelves using ICESat-2 (Walker & Gardner, 2019). We present observations from east to west along T1.

There were repeat acquisitions of RGT 1049 in September (three weeks pre-calving) and December (post-calving, Figure 2c). Prior to calving, this portion of the rift displayed uplifted wall flanks on the order of 1 m above surrounding terrain (Figure 2c). The post-calving profile captured in December demonstrates that the new ice front (former upstream rift wall) experienced an uplift of ~1 m. RGT 0607 (ascending) was sampled in cycle 2 (pre-pointing correction) and crossed over T1 at a nearly identical location as RGT 0721 (descending) in cycle 3 onward. Thus, the rift at that location was sampled on three occasions prior to calving, in February (0607), May and August (0721). Detrended profiles (Figure 2d) show that uplifted rift wall flanks rose almost 2 m above the un-rifted terrain, as expected for an active rift near the rift tip (Walker & Gardner, 2019). Further west, RGT 0279 crossed T1 along its track through the AIS suture zone, evident by the bumpy surface profiles (Figure 2e). This track was sampled three times in 2019: pre-calving in January (pre-pointing correction), April, and post-calving in October. Comparing pre- and post-calving topography in April (light blue) and October (green), the upstream rift shape appeared to remain unchanged, suggesting that pre-calving rift topography might influence ice front shape (see Section 4.3.3).

Based on its surface appearance in Landsat imagery pre-calving on September 12, 2019, T1 had not yet reached the location sampled by RGT 0668 in August 2019. Thus, RGT 1224 was the westernmost RGT to sample the *visible* rift prior to calving. It did so pre-calving in March and June, and in December 2019, 3 months post-calving. The cycle 02 track, prior to the pointing correction in March, was roughly 2.3 km east of the corrected pointing location sampled in June; the January profile therefore sampled a wider section of the rift. The June profile shows vertical uplift across the rift as a small, ~1 m wall flank signature at the center of the track (Figure 2f). In the last visible image prior to sunset in April 2019, T1 was ~40 m wide at that location, demonstrating the utility of ATL06 data (20 m posting) in observing rifts during Austral winter. The topography measured along the same track post-calving in December shows a similar shape post-calving, suggesting again that pre-calving topography along rifts modulates the new ice front shape.

Inspection of visible imagery placed the tip of T1 around the mid-point RGT 1224 and 0668 prior to sunset (Figure 1b). However, ICESat-2 detected it further west as a subtle surface depression in all six beams of RGT 0668 in August 2019 using both ATL06 and ATL03 (e.g., GT2L, Figure 2g and GT1L, Figure 2h). In each track, the rift manifested as a 0.5–1.5 m surface depression, with uplifted rift walls. This suggests that the rift was at least 6.1 km longer than visible images estimated in September 2019. A 1.24 m resolution WorldView-3 image (Figure 1c) from 04 September barely resolves the fracture on the ice shelf surface, ~268 m behind the rift tip detected in the 12 September Landsat image. This suggests that the rift tip we detected in the Landsat imagery is actually a shallow surface depression, rather than a fracture that had pierced the surface. When combined with the rift detection along RGT 0668 in August, this suggests that T1 propagated from below (basal fracture), and had not reached the surface yet. Thus, it had likely propagated much farther than we had been able to observe from the surface. Although our rift propagation records are still useful in terms of relative change over time, this inference may call into question the degree of iceberg detachment prior to the large propagation event between 12 and 25 September as observed in the imagery.

4.3.3. Changes in Amery Ice Front

ICESat and ROSETTA-Ice (airborne) altimetry data revealed a "rampart-moat" structure along icebergs that calved from the Ronne Ice Shelf and parts of the Ross Ice Shelf, respectively (Mosbeux et al., 2020; Scambos et al., 2005). This feature, which includes a several-meter-deep depression ("moat") typically <1 km inboard of a raised edge ("rampart"), is caused by wave-driven and thermal erosion of the front near the waterline, and the subsequent formation of a buoyant submerged bench of ice (Mosbeux et al., 2020; Scambos et al., 2005; Wagner et al., 2014, 2016). The resulting stress imbalance can eventually lead to the calving of a small "sliver-shaped iceberg" (Kristensen, 1983). The pre-calving ice front (Figure 1g) exhibits this shape, and is dimensionally similar to the rift flanking uplift. The rift uplift is preserved at the new ice front after the separation of D-28 (Figures 2i–2l). This suggests that the rift wall topography prior to calving modulates, or at least influences, the formation and/or resulting shape of the rampart-moat observed in more mature ice

fronts. In the case of the pre-calving rampart-moat structure observed along RGT 668 (Figure 2l), it appeared to be independent from the upstream surface topography, but it is likely any post-calving rampart-moat development will be superimposed on existing shape. The RGT 0279 Cycle 2 repeat (Figure 2k) shows apparent ∼6-m-high rampart-moat structure, but it is not clear whether this is the result of the suture zone topography or waterline erosion. As such, it is important to account for upstream topography such as that associated with rifts or suture zones when considering small-scale ice shelf calving driven by buoyant flexure.

5. Summary

We have used high resolution imagery and ICESat-2 data to analyze the first large iceberg calving event to occur during the ICESat-2 mission, D-28 from AIS on September 25, 2019. Propagation rates for three active AIS rifts (T1, T2, and E3) show that T1 propagated at an average rate of 5.1 m/day before calving, before experiencing an apparent rate increase to 1,842 m/day in the 12-day period between observations. We showed that the calving along T1 coincided with a large propagation burst in rift E3. This is consistent with the attribution of the calving event to strong offshore winds driven by anomalous twin polar cyclones over the western portion of the AIS front (Francis et al., 2020), likely having a mechanical effect on the rift itself, as also inferred by the high correlation between sustained winds (>4 days) and rift propagation by Walker et al. (2015). ICESat-2 data across T1 revealed uplifted rift wall flanks indicative of an active mode of propagation, which were preserved after calving. ICESat-2's 91-days cycle allowed repeat observations, even throughout winter. Its high resolution allowed for detection of the rift where it was not visible in Landsat-8 imagery, as a ∼1 m depression in the surface, ∼6.1 km farther advanced than it appeared in images acquired one month later. Even high resolution Worldview-3 images did not capture the extent of the rift detected by ICESat-2, suggesting that T1 propagates as a basal fracture and thus had already propagated much farther than we had been able to observe from the surface. This hypothesis is supported by the observed increase and divergence in flow velocity across T1 with time, suggesting that the nascent D-28 iceberg had been tearing away at an increasing rate during the past few years, and was likely decoupled from the upstream ice and intra-rift mélange. Overall, ICESat-2 has enabled us to investigate a tabular iceberg calving event in near-real time at unprecedented temporal and spatial resolution.

Data Availability Statement

A list of all data and how to download it, and all code needed to produce the figures in this analysis are available on GitHub for the purpose of peer review: https://github.com/PolarCatCCW/amery_rifts_D28.

References

Adusumilli, S., Fricker, H. A., Medley, B., Padman, L., & Siegfried, M. R. (2020). Interannual variations in meltwater input to the Southern Ocean from Antarctic ice shelves. *Nature Geoscience*, *13*(9), 616–620. https://doi.org/10.1038/s41561-020-0616-z

Bassis, J. N., Coleman, R., Fricker, H. A., & Minster, J. B. (2005). Episodic propagation of a rift on the Amery ice shelf, East Antarctica. *Geophysical Research Letters*, *32*(6), L06502. https://doi.org/10.1029/2004GL022048

Bassis, J. N., Fricker, H. A., Coleman, R., & Minster, J. B. (2008). An investigation into the forces that drive ice-shelf rift propagation on the Amery ice shelf, East Antarctica. *Journal of Glaciology*, *54*(184), 17–27. https://doi.org/10.3189/002214308784409116

Benn, D. I., & Åström, J. A. (2018). Calving glaciers and ice shelves. *Advances in Physics X*, *3*(1), 1513819. https://doi.org/10.1080/23746149.2018.1513819

Benn, D. I., Warren, C. R., & Mottram, R. H. (2007). Calving processes and the dynamics of calving glaciers. *Earth-Science Reviews*, *82*(3), 143–179. https://doi.org/10.1016/j.earscirev.2007.02.002

Borstad, D. Mc Grath, & Pope, A. (2017). Fracture propagation and stability of ice shelves governed by ice shelf heterogeneity. *Geophysical Research Letters*, *44*(9), 4186–4194. https://doi.org/10.1002/2017GL072648

Bromirski, P. D., Sergienko, O. V., & MacAyeal, D. R. (2010). Transoceanic infragravity waves impacting Antarctic ice shelves. *Geophysical Research Letters*, *37*(2), L06502. https://doi.org/10.1029/2009GL041488

Brunt, K. M., Neumann, T. A., & Smith, B. E. (2019). Assessment of ICESat-2 ice sheet surface heights, based on comparisons over the interior of the Antarctic ice sheet. *Geophysical Research Letters*, *46*(22), 13072–13078. https://doi.org/10.1029/2019GL084886

Brunt, K., Okal, E., & MacAyeal, D. (2011). Antarctic ice-shelf calving triggered by the Honshu (Japan) earthquake and tsunami, March 2011. *Journal of Glaciology*, *57*, 785–788. https://doi.org/10.3189/002214311798043681

Budd, W. (1966). The Dynamics of the Amery ice shelf. *Journal of Glaciology*, *6*(45), 335–358. https://doi.org/10.3189/S0022143000019456

Francis, D., Mattingly, K. S., Lhermitte, S., Temimi, M., & Heil, P. (2020). Atmospheric extremes triggered the biggest calving event in more than 50 years at the Amery ice shelf in September 2019. *The Cryosphere Discussions*, *2020*, 1–30. https://doi.org/10.5194/tc-2020-219

Fricker, H. A., Bassis, J. N., Minster, B., & MacAyeal, D. R. (2005). ICESat's new perspective on ice shelf rifts: The vertical dimension. *Geophysical Research Letters*, *32*(23), L23S08. https://doi.org/10.1029/2005GL025070

Fricker, H. A., Young, N. W., Allison, I., & Coleman, R. (2002). Iceberg calving from the Amery ice shelf, East Antarctica. *Annals of Glaciology*, *34*, 241–246. https://doi.org/10.3189/172756402781817581

Fricker, H. A., Young, N., Coleman, R., Bassis, J. N., & Minster, J. B. (2005b). Multi-year monitoring of rift propagation on the Amery Ice Shelf. *East Antarctica*, *32*, L02502. https://doi.org/10.1029/2004GL021036

Gardner, A. S., Fahnestock, M. A., & Scambos, T. A. (2019). *ITS_LIVE regional glacier and ice sheet surface velocities*. Boulder, CO: National Snow and Ice Data Center. https://doi.org/10.5067/6II6VW8LLWJ7

Gudmundsson, G. H., Paolo, F. S., Adusumilli, S., & Fricker, H. A. (2019). Instantaneous Antarctic ice sheet mass loss driven by thinning ice shelves. *Geophysical Research Letters*, *46*(23), 13903–13909. https://doi.org/10.1029/2019GL085027

Heeszel, D. S., Fricker, H. A., Bassis, J. N., O'Neel, S., & Walter, F. (2014). Seismicity within a propagating ice shelf rift: The relationship between icequake locations and ice shelf structure. *Journal of Geophysical Research: Earth Surface*, *119*(4), 731–744. https://doi.org/10.1002/2013JF002849

Hulbe, C. L., LeDoux, C., & Cruikshank, K. (2010). Propagation of long fractures in the Ronne ice shelf, Antarctica, investigated using a numerical model of fracture propagation. *Journal of Glaciology*, *56*(197), 459–472. https://doi.org/10.3189/002214310792447743

Humbert, A., & Steinhage, D. (2011). The evolution of the western rift area of the Fimbul Ice Shelf, Antarctica. *The Cryosphere*, *5*(4), 13.

Joughin, I., & MacAyeal, D. R. (2005). Calving of large tabular icebergs from ice shelf rift systems. *Geophysical Research Letters*, *32*(2), L02501. https://doi.org/10.1029/2004GL020978

Kristensen, M. (1983). Iceberg calving and deterioration in Antarctica. *Progress in Physical Geography: Earth and Environment*, *7*(3), 313–328. https://doi.org/10.1177/030913338300700301

Kulessa, B., Booth, A. D., O'Leary, M., McGrath, D., King, E. C., Luckman, A. J., et al. (2019). Seawater softening of suture zones inhibits fracture propagation in Antarctic ice shelves. *Nature Communications*, *10*(1), 5491. https://doi.org/10.1038/s41467-019-13539-x

Kulessa, B., Jansen, D., Luckman, A. J., King, E. C., & Sammonds, P. R. (2014). Marine ice regulates the future stability of a large Antarctic ice shelf. *Nature Communications*, *5*(1), 3707. https://doi.org/10.1038/ncomms4707

Larour, E., Rignot, E., & Aubry, D. (2004). Modelling of rift propagation on Ronne ice shelf, Antarctica, and sensitivity to climate change. *Geophysical Research Letters*, *31*(16), L16404. https://doi.org/10.1029/2004GL020077

Lipovsky, B. P. (2018). Ice Shelf Rift Propagation and the Mechanics of Wave-Induced Fracture. *Journal of Geophysical Research: Oceans*, *123*(6), 4014–4033. https://doi.org/10.1029/2017JC013664

MacAyeal, D. R., Okal, E. A., Aster, R. C., Bassis, J. N., Brunt, K. M., Cathles, L. M., et al. (2006). Transoceanic wave propagation links iceberg calving margins of Antarctica with storms in tropics and Northern Hemisphere. *Geophysical Research Letters*, *33*(17), L17502. https://doi.org/10.1029/2006GL027235

MacAyeal, D. R., Okal, E. A., Aster, R. C., & Bassis, J. N. (2017). Seismic observations of glaciogenic ocean waves (micro-tsunamis) on icebergs and ice shelves. *Journal of Glaciology*, *55*(190), 193–206. https://doi.org/10.3189/002214309788608679

MacGregor, J. A., Catania, G. A., Markowski, M. S., & Andrews, A. G. (2012). Widespread rifting and retreat of ice-shelf margins in the eastern Amundsen Sea Embayment between 1972 and 2011. *Journal of Glaciology*, *58*(209), 458–466. https://doi.org/10.3189/2012JoG11J262

Martino, A. J., Neumann, T. A., Kurtz, N. T., & McLennan, D. (2019). ICESat-2 mission overview and early performance. *Proc. SPIE 11151, Sensors, Systems, and Next-Generation Satellites XXIII*, 111510C. https://doi.org/10.1117/12.2534938

Mosbeux, C., Wagner, T. J. W., Becker, M. K., & Fricker, H. A. (2020). Viscous and elastic buoyancy stresses as drivers of ice-shelf calving. *Journal of Glaciology*, *66*(258), 643–657. https://doi.org/10.1017/jog.2020.35

Neumann, T. A., Brenner, A. C., Hancock, D., Robbins, J., Saba, J., Harbeck, K., et al. (2020). ATLAS/ICESat-2 L2A global geolocated photon data, Version 3. Boulder, CO: National Snow and Ice Data Center. https://doi.org/10.5067/ATLAS/ATL03.001

Paolo, F. S., Fricker, H. A., & Padman, L. (2015). Volume loss from Antarctic ice shelves is accelerating. *Science*, *348*(6232), 327. https://doi.org/10.1126/science.aaa0940

Rignot, E., Jacobs, S., Mouginot, J., & Scheuchl, B. (2013). Ice-Shelf melting around Antarctica. *Science*, *341*(6143), 266.

Scambos, T. A., Sergienko, O., Sargent, A., MacAyeal, D. R., & Fastook, J. (2005). ICES at profiles of tabular iceberg margins and iceberg breakup at low latitudes. *Geophysical Research Letters*, *32*(23), L23S09. https://doi.org/10.1029/2005GL023802

Sergienko, O. V. (2010). Elastic response of floating glacier ice to impact of long-period ocean waves. *Journal of Geophysical Research*, *115*(F4), F04028. https://doi.org/10.1029/2010JF001721

Smith, B., Fricker, H. A., Gardner, A. S., Medley, B., Nilsson, J., Paolo, F. S., et al. (2020). Pervasive ice sheet mass loss reflects competing ocean and atmosphere processes. *Science*, *368*(6496). https://doi.org/10.1126/science.aaz5845

Smith, B., Fricker, H. A., Gardner, A. S., Siegfried, M. R., Adusumilli, S., Csathó, B., et al. (2020). *ATLAS/ICESat-2 L3A Land Ice Height, Version 3*. Boulder, CO: NSIDC: National Snow and Ice Data Center.

Thomas, R. H. (1979). The dynamics of marine ice sheets. *Journal of Glaciology*, *24*(90), 167–177. https://doi.org/10.3189/S0022143000014726

Wagner, T. J. W., James, T. D., Murray, T., & Vella, D. (2016). On the role of buoyant flexure in glacier calving. *Geophysical Research Letters*, *43*(1), 232–240A. https://doi.org/10.1002/2015GL067247

Wagner, T. J. W., Wadhams, P., Bates, R., Elosegui, P., Stern, A., Vella, D., et al. (2014). The "footloose" mechanism: Iceberg decay from hydrostatic stresses. *Geophysical Research Letters*, *41*(15), 5522–5529. https://doi.org/10.1002/2014GL060832

Walker, C. C., Bassis, J. N., Fricker, H. A., & Czerwinski, R. J. (2013). Structural and environmental controls on Antarctic ice shelf rift propagation inferred from satellite monitoring. *Journal of Geophysical Research: Earth Surface*, *118*(4), 2354–2364. https://doi.org/10.1002/2013JF002742

Walker, C. C., Bassis, J. N., Fricker, H. A., & Czerwinski, R. J. (2015). Observations of interannual and spatial variability in rift propagation in the Amery Ice Shelf, Antarctica 2002–14, *Journal of Glaciology*, *26*, 243–252. https://doi.org/10.3189/2015JoG14J151

Walker, C. C., & Gardner, A. S. (2019). Evolution of ice shelf rifts: Implications for formation mechanics and morphological controls. *Earth and Planetary Science Letters*, *526*, 115764. https://doi.org/10.1016/j.epsl.2019.115764